JOURNAL OF GEOPHYSICAL RESEARCH, VOL. 91, NO. B2, PAGES 1961–1974, FEBRUARY 10, 1986

Convection Beneath Young Oceanic Lithosphere: Implications for Thermal Structure and Gravity

W. ROGER BUCK[1]

Department of Earth, Atmospheric, and Planetary Sciences, Massachusetts Institute of Technology, Cambridge

E. M. PARMENTIER

Department of Geological Sciences, Brown University, Providence, Rhode Island

Small-scale convection under the oceanic lithosphere which begins in the first 5 m.y. of cooling can produce a gravity signal with the amplitude and wavelength observed for large areas of the central Pacific and southern Indian oceans using Seasat altimeter data. The trend of the observed anomalies is parallel to the direction of plate motion as might be expected if they were produced by small-scale convection. Models predict that the wavelengths of gravity anomalies increase more rapidly with age than is observed. The persistence of short relatively uniform wavelength anomalies (< 200 km) to crustal ages of 50 Ma may indicate that they were produced when the lithosphere was very young and thin and were "frozen in" as cooling thickened the elastic lithosphere. Small-scale convection which begins under very young lithosphere does not violate other geophysical data such as the rate of seafloor subsidence and variations of geoid height with age. After convection has begun, the subsidence due to thermal contraction within the lithosphere varies linearly with age, in the absence of mantle heat sources, although the rate of change of these quantities is affected by convection. Much of the variation of the geoid height across fracture zones can be fit by a model which includes small-scale convection.

INTRODUCTION

Convection beneath the oceanic plates on a scale smaller than the horizontal dimensions of the lithospheric plates has been suggested to explain several geophysical observables. This provides one suggested explanation for the deviation of seafloor subsidence with age from that predicted by simple conductive cooling of the oceanic lithosphere [*Parsons and McKenzie*, 1978]. More recently, in their analysis of Seasat altimeter data, *Haxby and Weissel* [1986] have noted linear gravity anomalies which trend in the direction of plate motion. They have suggested that these features may be the result of small-scale convection. Based on theoretical considerations, *Richter* [1973] predicted that small-scale convection should take the form of two-dimensional rolls with axes oriented in the direction of plate motion, thus providing an explanation for the form of the observed gravity anomalies. In this paper we describe numerical calculations aimed at understanding small-scale flow which may occur under the oceanic plates. The purpose of this work is to investigate whether models which are consistent with subsidence-age data for the oceans and other geophysical data can produce the observed gravity features.

We first review previous work on small-scale convection and then discuss the formulation of approximate models of convection and the calculation of several geophysical observables predicted by the models. A range of models is considered based on laboratory measurements of physical properties of mantle minerals and estimates of mantle viscosity. The predictions of the models are compared with data for subsidence of the ocean floor and gravity for the oceans.

A number of investigations have been carried out on the effect of shearing on the form of thermal convective instabilities, including early experimental work by *Graham* [1933] and theoretical stability studies by *Ingersoll* [1966] and *Gage and Reid* [1968]. *Richter* [1973] showed that finite amplitude convective motions in an infinite Prandtl number fluid could be reoriented by shearing and suggested that large-scale mantle flow associated with plate motions could control the form of small-scale convection beneath a plate. This was corroborated by the laboratory experiments of *Richter and Parsons* [1975] and *Curlet* [1976].

Theoretical studies of the stability of the top thermal boundary layer of the large-scale mantle flow have also been carried out [*Parsons and McKenzie*, 1978; *Jaupart*, 1981; *Yuen et al.*, 1981; *Yuen and Fleitout*, 1984]. *Parsons and McKenzie* [1978] treated a mantle of uniform viscosity below a fixed boundary and found that a thermal boundary layer could go unstable after 70 m.y. of cooling if its viscosity were $\sim 10^{21}$ Pa s. *Yuen et al.* [1981] considered a viscosity structure resulting only from temperature-dependent viscosity. For viscosities which depend only on temperature and which are consistent with postglacial rebound estimates of whole mantle viscosity, they conclude that no instabilities develop in a cooling boundary layer for a time equal to the age of the oldest oceanic plates (200 Ma). *Jaupart and Parsons* [1985] studied the linear stability problem for a depth-dependent viscosity structure and concluded that for the base of the oceanic lithosphere to go unstable after 70 m.y. of conductive cooling required average viscosities there of the order of 10^{21} Pa s. They also noted that the ratio of the maximum to the minimum viscosity in the convecting region was at most about a factor of 10. *Yuen and Fleitout* [1984] concluded that viscosity which depends on pressure as well as temperature is required to allow boundary layer average viscosities to be low enough for small-scale convection to occur under the ocean plates (i.e., a low-viscosity zone) and still match other constraints on mantle viscosity. Our first finite amplitude calculations [*Buck*, 1983] led to the same conclusion.

Two previous studies which have considered the time evolu-

[1] Now at Lamont-Doherty Geological Observatory of Columbia University, Palisades, New York.

Paper number 5B5483.
0148-0227/86/005B-5483$05.00

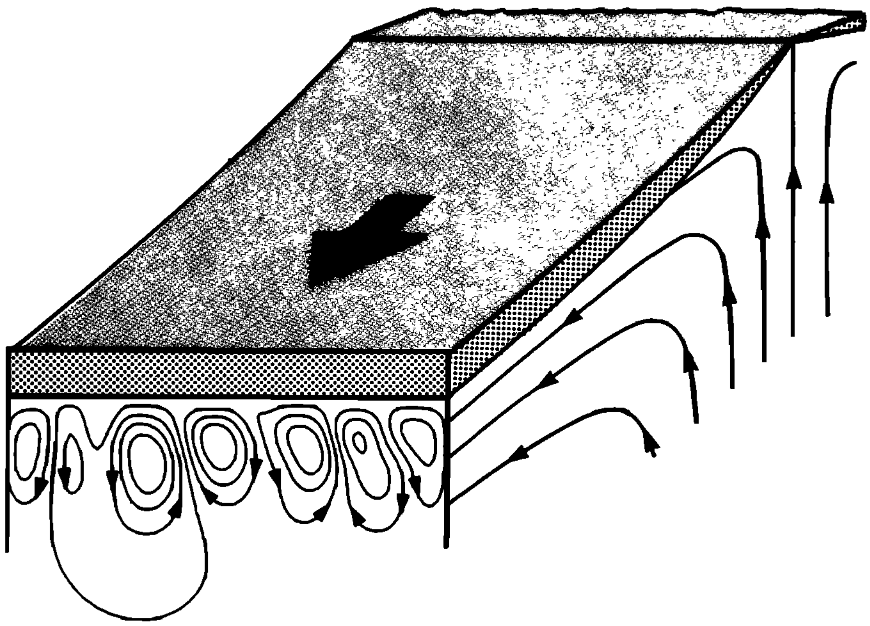

Fig. 1. Small-scale convection beneath the oceanic lithosphere having the form of rolls oriented in the direction of plate motion. Flow in a vertical plane parallel to the ridge (spreading center) axis is calculated from a two-dimensional, transient convective cooling model with boundary conditions shown in Figure 2. The streamlines shown are from Figure 3*b* at a time (lithosphere age) of 9 Ma.

tion of convection are similar in formulation to the present work [*Houseman and McKenzie*, 1982; *Fleitout and Yuen*, 1984]. Both studies are concerned with the possibility that small-scale convection can explain a decrease in the rate of seafloor subsidence after an age of about 70 Ma. The formulation of Houseman and McKenzie cannot allow for the motion of the boundary between the lithosphere and the convecting region below because they treat a convecting region with constant viscosity and a rigid lithosphere. In their model the boundary layer could not go unstable until cooling had penetrated through the rigid lithosphere. *Fleitout and Yuen* [1984] considered a temperature- and pressure-dependent viscosity, thus avoiding the need to define a lithosphere of constant thickness. However, the wavelength and depth of penetration of the flow were prescribed, and little variation of the viscosity parameters was considered. Because these studies were concerned with the approach of the lithosphere to a thickness in equilibrium with the background mantle heat flux, convection was driven by both heating from below and heating from within.

The purpose of this study is to calculate the effect of small-scale convection on the cooling of oceanic lithosphere which is less than 70 Ma in age. We consider viscosities which are in accord with laboratory and geophysical estimates for the mantle. A wide range of viscosity parameters were studied in order to estimate the sensitivity of the convecting system and to identify the values which can match geophysical data on oceanic lithosphere. In our formulation the boundary layers can go unstable and convection begin at a time which is determined by the viscosity parameters. In our problem the lithosphere and the convecting region are allowed to interact, and the thickness of the lithosphere changes with time. We consider the viscosity to be temperature- and pressure-dependent, but we do not constrain the wavelength and depth of penetration of the convection in some of the calculations. In the first 40–70 m.y. of lithospheric cooling, heat sources in the mantle should have a small effect on the rate of cooling. Therefore heat sources are not included in these models.

MODEL FORMULATION

Small-scale convection in the form of rolls with axes parallel to the direction of plate motion is illustrated in Figure 1. As in previous studies [*Houseman and McKenzie*, 1982; *Fleitout and Yuen*, 1984], we simplify the three-dimensional problem to consider only two-dimensional flow in a vertical plane parallel to a ridge crest. In doing so, we ignore the effect of vertical gradients in horizontal velocity perpendicular to the ridge and both the thermal and mechanical coupling between vertical planes parallel to the ridge. As a result of this assumption, the effect of vertical shearing by plate motion on the thermal and mechanical structure is also ignored. These approximations reduce the problem to one of time-dependent two-dimensional convection. The plane of the calculation is considered to move with the plate, so model time corresponds to the age of oceanic lithosphere and is proportional to distance from the ridge crest.

The depth of penetration of the small-scale cells into the mantle must depend in part on the structure of the large-scale flow. Here, we consider no penetration deeper than 400 km since we are mainly concerned with the effects of small-scale convection soon after it has begun, when the cells are of small vertical scale. For greater penetration depths, the interaction of the large- and small-scale flow will almost certainly be more complicated than we assume here. Also the gravity anomalies described by *Haxby and Weissel* [1986] generally have wavelengths of about 200 km. The depth of penetration of convection cells should be of the same order as the wavelength of the gravity anomalies they produce, as will be seen in the model results.

With these assumptions and simplifications our problem reduces to studying thermal convection in a box of variable viscosity fluid driven by cooling from above. This box is shown in Figure 2. We define a region of calculation (or box) to be of width L and depth D. In that region we solve the two-dimensional Navier-Stokes equations for mass, momentum, and energy conservation [*Batchelor*, 1967]. They are modified for flow in the earth's mantle by dropping inertia terms and terms that depend on material compressibility [*Turcotte et al.*, 1973]. The values of the physical parameters which were used are given in Table 1.

The governing equations were solved using finite difference approximations with centered differences for the diffusion terms and upwind differences for the advection terms. Forward time stepping was used for the time derivatives. We used variable spacing of grid points in a difference scheme developed by *Parmentier* [1975]. This allowed higher resolution in the regions of the largest gradients of viscosity and flow, without an excessive number of points overall. In the region of highest resolution the grid spacing is uniform, so formal second-order accuracy in the centered difference approximations is preserved [*Roache*, 1982]. The grid point positions are shown in Figures 3 and 4 as marks around the boxes.

Resolution of the solutions on the grids used here was established in two ways. First, the numerical experiments were done on successively refined grids until the same results were achieved on two different grids. Second, the heat flux out of the grid was compared to the average rate of change of temperature within the box to ensure conservation of energy. Cases 12 and 20, described later and in Table 2, were identical except that the number of grid points in each direction was greater by a factor of 1.5 for case 20. The maximum difference in average temperature (Figure 5) was less than 5%.

Since olivine is considered to be the dominant mineral in the upper mantle [*Ringwood*, 1975], we adopt a relation for the dynamic viscosity μ [*Weertman and Weertman*, 1975] given by

$$\mu(T, P) = A \exp((E + PV)/RT) \qquad (1)$$

where E is the activation energy, V is the activation volume, A is a constant varied to adjust the average viscosity, and R is the universal gas constant. The value of the activation energy, which controls the temperature dependence of the viscosity, is estimated from laboratory data. *Geotze* [1978] summarizes measurements of creep in olivine giving 520 ± 20 kJ/mol as a value for E. Based on dislocation recovery during static annealing, *Kohlstedt et al.* [1980] find that $E = 300 \pm 20$ kJ/mol. We generally use values intermediate to these. The temperature fields displayed later do not include an adiabatic gradient, but the temperatures used to calculate the viscosity from

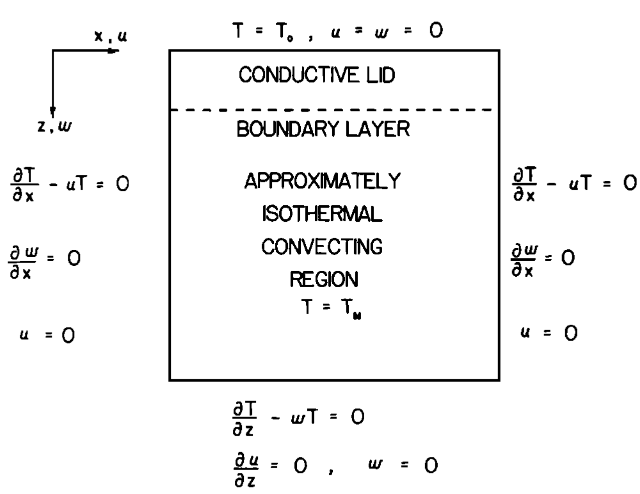

Fig. 2. The boundary conditions for the numerical experiments described in this paper. The conductive lid is the region where the advective heat flux is negligible compared to the conductive heat flux. The convective boundary layer is defined in the text as are the boundary conditions.

TABLE 1. Parameters Used for Nondimensionalizing the Governing Equations and Calculating the Model Results

Symbol	Name	Value	Units
κ	diffusivity	10^{-6}	m²/s
L	length scale	4.0×10^5	m
ΔT	temperature scale	1300	°C
α	thermal expansion coefficient	3.0×10^{-5}	1/°C
μ	viscosity	1.0×10^{21}	Pa s
g	acceleration of gravity	9.8	m/s²
ρ_m	mantle density	3500	kg/m³
ρ_w	water density	1000	kg/m³
K	conductivity	3.2	J/m s °C
c_p	specific heat	900	J/kg °C

equation (1) did include a contribution due to an adiabatic gradient of 0.3°C/km. *Sammis et al.* [1981] show that estimates of the activation volume based on both experimental and theoretical methods give a range for olivine of 10–20 $\times 10^{-5}$ m³/mol. The activation volume, which controls the pressure dependence of the viscosity, is critical to reconciling different estimates of mantle viscosity based on geophysical observations.

An average mantle viscosity of about 10^{21} Pa s is required by postglacial rebound [*Cathles*, 1975; *Peltier and Andrews*, 1976]. Several geophysical observations require much lower viscosities at shallow depths in the mantle under the oceanic lithosphere and under tectonically active regions of the continents. *Passey* [1981] has analyzed the rebound of dried lakes in Utah and infers shallow mantle viscosities lower than 10^{19} Pa s. *Richter and McKenzie* [1978] and *Weins and Stein* [1985] require asthenospheric viscosities beneath the oceans in the range of 10^{18}–10^{19} Pa s based on the distribution of stresses in the oceanic plates. Viscosity must increase with pressure and therefore depth to reconcile low viscosities at shallow depths and higher average viscosities for the mantle. Figures 3 and 4 show viscosity calculated with equation (1) plotted versus depth for the viscosity parameters given in Table 2.

At the top of a cooling variable viscosity fluid, temperatures are low and temperature gradients are high. Therefore viscosity, given by equation (1), in the top of the box can be so large that flow is negligible in that region. In this lid, which is analogous to the thermal lithosphere, heat transfer takes place exclusively by conduction. Below this region convection is the dominant mechanism of heat transport. Since we are considering the transient cooling of a fluid and not a steady state condition, both the lid thickness and the vigor of the convection in the interior will change with time. It is the interaction of the cooling, thickening lid with the underlying convecting region which is of interest. The convection is driven by the temperature gradients at the base of the lid, and in turn the rate of thickening of the lid (or lithosphere) is affected by the convection.

Boundaries on all sides of the box are taken to be shear stress-free. However, it is computationally more efficient to place a no-slip (fixed) boundary at the depth in the lid where viscosity is three orders of magnitude above the minimum viscosity in the box. Because the viscosity is so high in the cold lid, there is effectively no flow there. Calculations with the boundary at shallower depth in the lithosphere, where the viscosity is higher, give the same results but require more computer time. The thermal boundary conditions are fixed temperature (0°C) at the top and insulating on the sides and

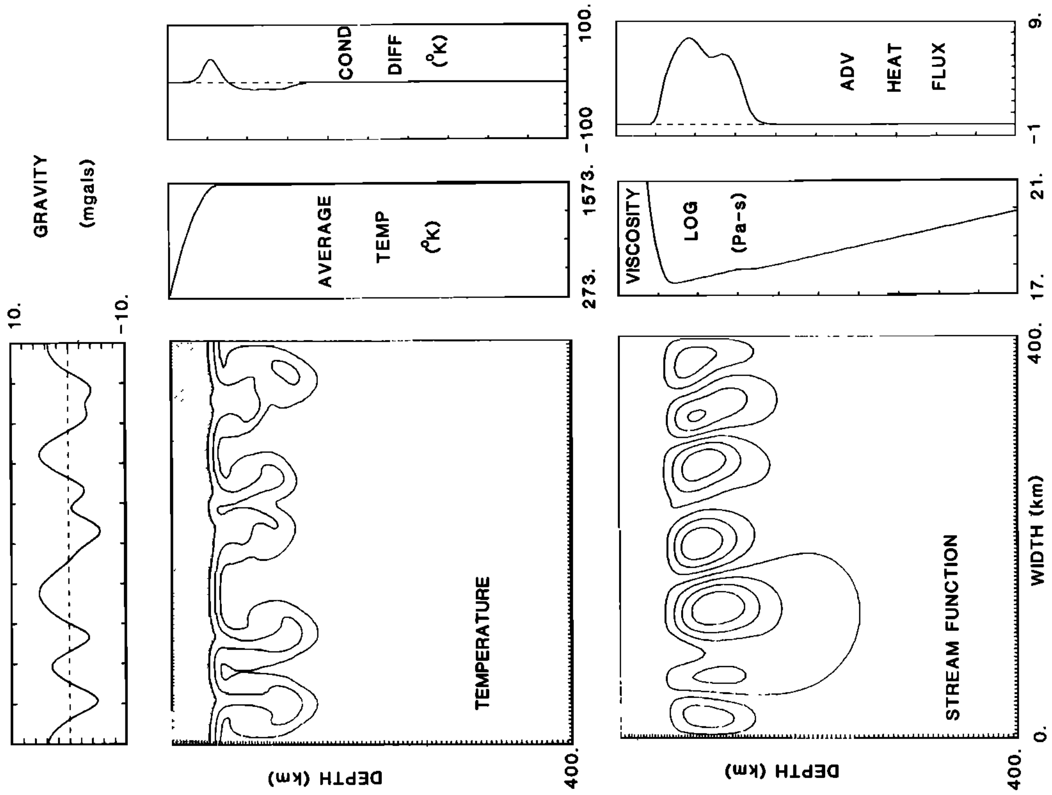

GRAVITY
(mgals)
10.
-10.
TEMPERATURE
DEPTH (km)
400.
AVERAGE
TEMP
(°K)
273.
1573.
COND
DIFF
(°K)
-100
100.
VISCOSITY
LOG
(Pa-s)
17.
21.
ADV
HEAT
FLUX
-1
9.
STREAM FUNCTION
DEPTH (km)
400.
0.
WIDTH (km)
400.

Fig. 3b

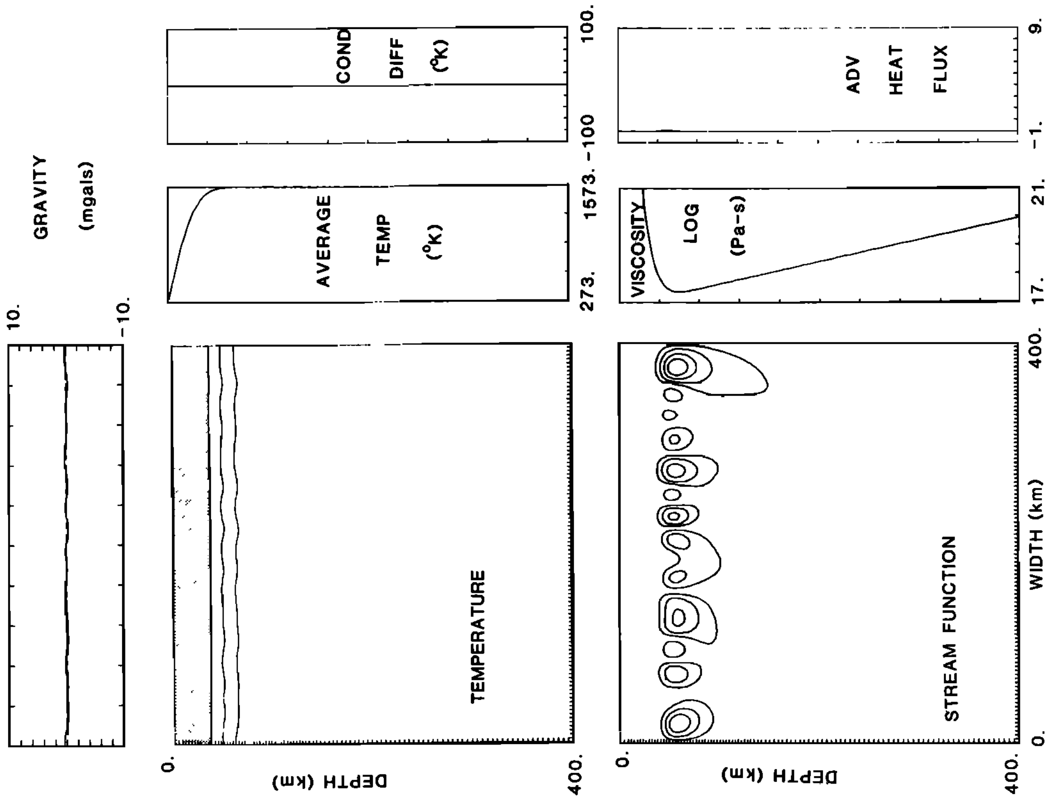

GRAVITY
(mgals)
10.
-10.
0.
TEMPERATURE
DEPTH (km)
400.
AVERAGE
TEMP
(°K)
273.
1573.
COND
DIFF
(°K)
-100
100.
VISCOSITY
LOG
(Pa-s)
17.
21.
ADV
HEAT
FLUX
-1.
9.
0.
STREAM FUNCTION
DEPTH (km)
400.
0.
WIDTH (km)
400.

Fig. 3a

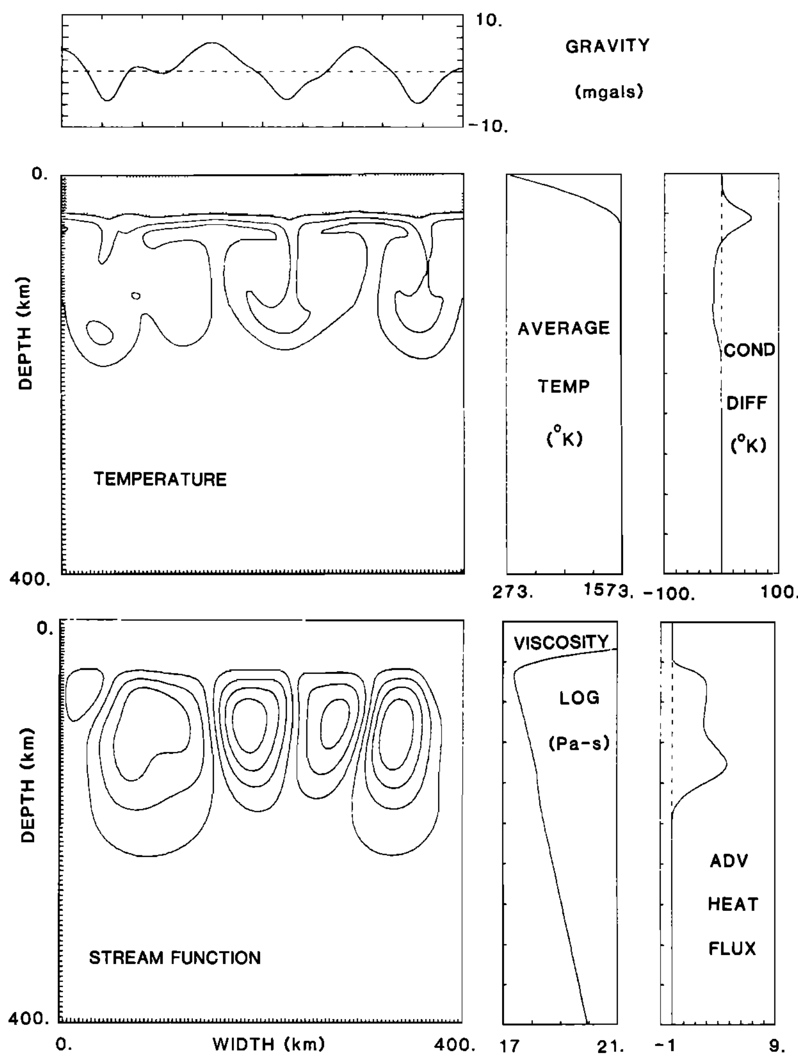

Fig. 3c

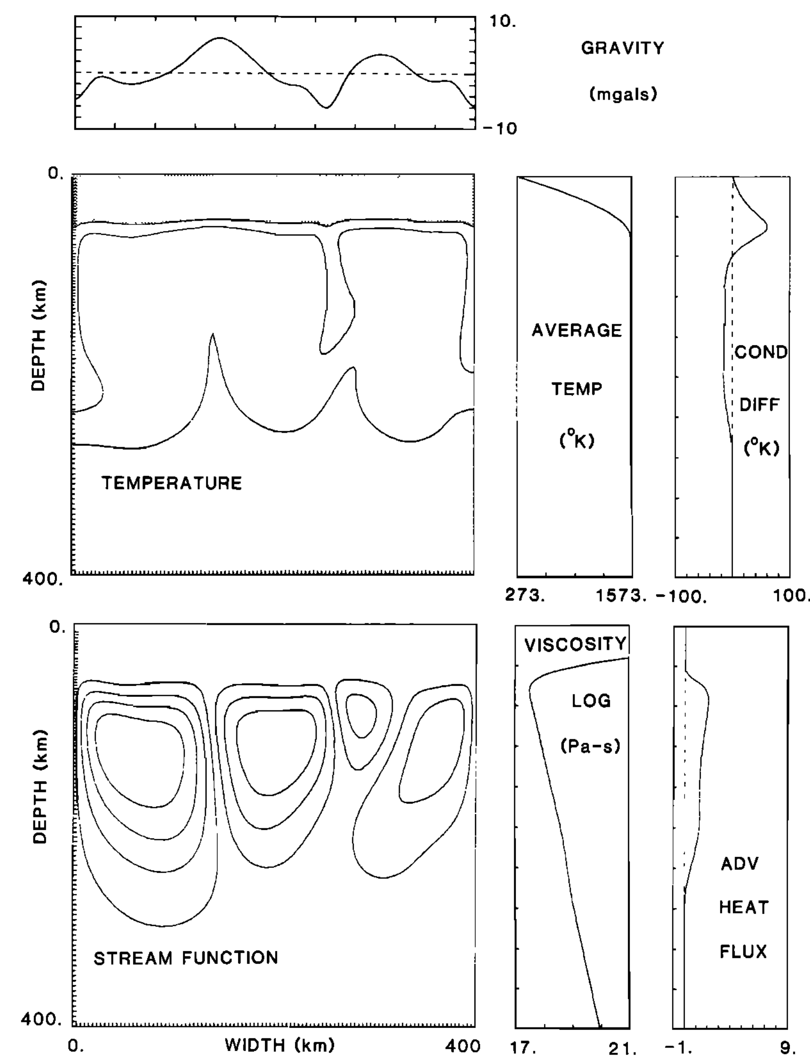

Fig. 3d

Fig. 3. The results of one numerical experiment (case 15) of small-scale convection within a box which represents a 400 × 400 km region of the mantle. Times of (*a*) 2, (*b*) 4, (*c*) 5, and (*d*) 10 m.y. after the calculation was begun. An initial temperature profile from 5 Ma of conductive cooling was used so that the above times correspond to 7, 9, 10, and 15 m.y. lithosphere ages. A random temperature perturbation was introduced at the start of the calculation. The dominant wavelength of flow increases from about 80 km after 2 m.y. to 200 km after 10 m.y. The isotherms correspond to temperatures of 1200°, 1250°, and 1280°C, in order from the top, and the streamlines are evenly spaced between maximum and minimum values. The shaded region above the uppermost isotherm is the conductive lid or lithosphere. The horizontally averaged temperature and its deviation (COND DIFF) from that for purely conductive cooling of a half-space at the same time are shown. The horizontal average of the viscosity and the vertically advected heat flux (ADV HEAT FLUX) are shown. The model gravity anomaly shown includes the effect of temperature variations and the vertical deformations produced by the flow, assuming no flexural damping. The positions of the grid points are indicated by the tick marks on the sides of the boxes.

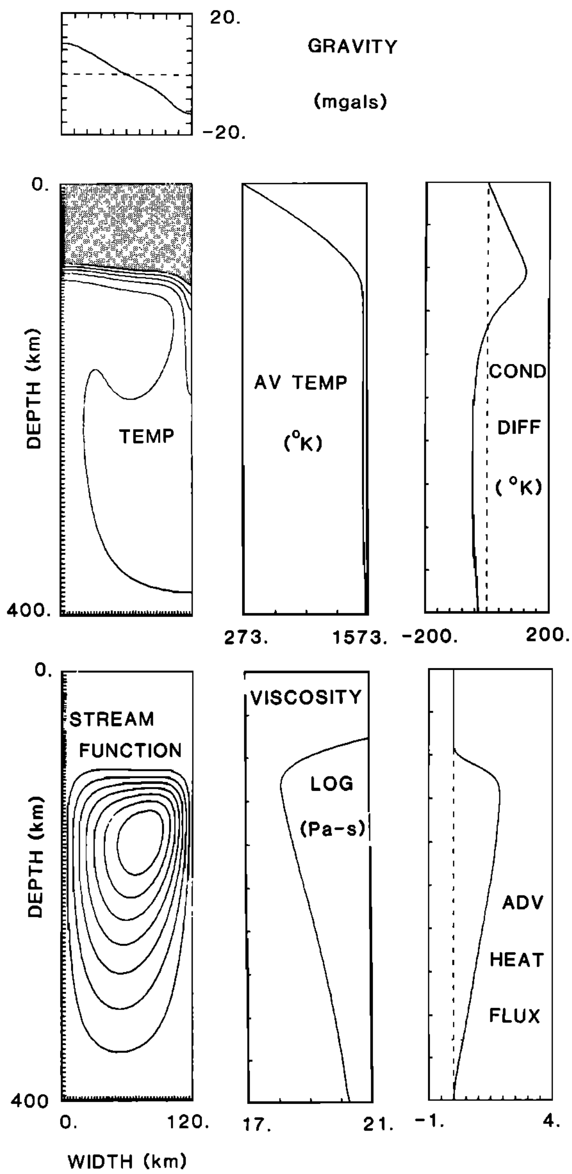

Fig. 4. The same quantities as in Figure 3 for case 20 at a time 56 m.y. into the calculation. The isotherms correspond to temperatures of 1160°, 1185°, 1210°, and 1235°C in order from top to bottom.

bottom. Both thermal and stress boundary conditions on the vertical sides are equivalent to a reflection condition.

A horizontally uniform initial temperature resulting from 5 m.y. of conductive cooling with an initial box temperature T_m of 1300°C is adopted. Convection may begin earlier than this for some of the viscosity structures we examine, but temperature and viscosity gradients are so large at smaller times that they are difficult to resolve even on relatively fine grids. To induce convective motion, two types of initial temperature perturbations are superimposed on the horizontally uniform temperature profile. In the first, a random perturbation of less than 1°C was introduced at each grid point. In the second, a periodic temperature perturbation with a wavelength equal to twice the width of the box and with a 1°C amplitude was used to induce the growth of only one convective wavelength.

A list of the model parameters which are common to all the numerical experiments is given in Table 1. The average viscosity (expressed as a reference viscosity and controlled by parameter A), the activation energy E, the activation volume V, the width L, and depth D of the box are varied from one calculation to another, as listed in Table 2. A random initial temperature perturbation was used in only one of the models. This is case 15 which was also carried out in the widest box. This model is designed to examine changes in the depth of penetration and wavelength of the convection cells with time. In the other model cases only one convection cell is induced by a periodic temperature perturbation. These smaller, simpler cases are used to study the effect of varying parameters and to examine the effects of different convective wavelengths.

Calculations with non-Newtonian viscosity have been carried out but are not discussed in detail here. Using nearly the same parameters for stress dependence of viscosity as *Fleitout and Yuen* [1984], we found no effect on our calculations. In their formulation, below a deviatoric stress of 10 bars the viscosity is Newtonian. The deviatoric stresses in our calculations are generally less than this value because the convective wavelengths are small.

The box can be divided into three regions based on the mode of heat transfer: a conductive lid, a convective thermal boundary layer, and a nearly isothermal convecting region (see Figure 2). The top of the convecting region is defined as the level of maximum horizontally averaged advective heat flux Q:

$$Q(z) = \frac{1}{L}\int_0^L w(x, z)T(x, z)\, dx \tag{2}$$

where w is the vertical component of the velocity. The convecting region is considered to be all the area at greater depth where the temperature is nearly uniform. In the conductive lid, the advective heat flux is effectively zero. This region extends to a depth where the average temperature exceeds 90% of that in the convecting region. Thus we define the base of the lid Z_L to correspond to this temperature. The average temperature in the conductive lid T_L is defined as

$$T_L = \frac{1}{LZ_L}\int_0^{Z_L}\int_0^L T(x, z)\, dx\, dz \tag{3}$$

Figure 5 shows values of T_L for a number of the calculations.

We consider the lithosphere to be analogous to the conductive lid and calculate the seafloor subsidence due to vertical thermal contraction and isostatic equilibrium. In terms of T_L, the subsidence is given by

$$S(t) = \left(\frac{\alpha\rho_m}{\rho_m - \rho_w}\right)(T_m - T_L)Z_L \tag{4}$$

Both subsidence and Z_L are plotted as a function of $t^{1/2}$ in Figure 6 for two of the cases. Since the average temperature of

TABLE 2. Parameters Which Define the Numerical Cases

Case	μ_{ref}, 10^{18} Pa s	E, kJ/mol	V, cm^3/mol	L, km	D, km	λ	Number of Grid Points
12	1.0	420	10.0	120	400	0.80	2,320
14	5.0	420	10.0	120	400	0.93	2,320
15	1.0	420	10.0	400	400	0.87	10,201
17	0.5	420	2.5	120	400	0.74	2,320
18	5.0	300	10.0	120	400	0.78	2,320
19	1.0	420	10.0	120	400	0.79	4,400
20	1.0	420	10.0	120	400	0.81	4,400
21	0.5	420	2.5	120	400	···	4,400
22	1.0	420	10.0	60	400	0.80	4,400
23	1.0	420	10.0	120	300	0.84	3,560

The reference viscosity μ_{ref}, the value of viscosity at the start of a calculation at 150 km depth in the model box, defines the value of A in equation (1). The other parameters are described in the text.

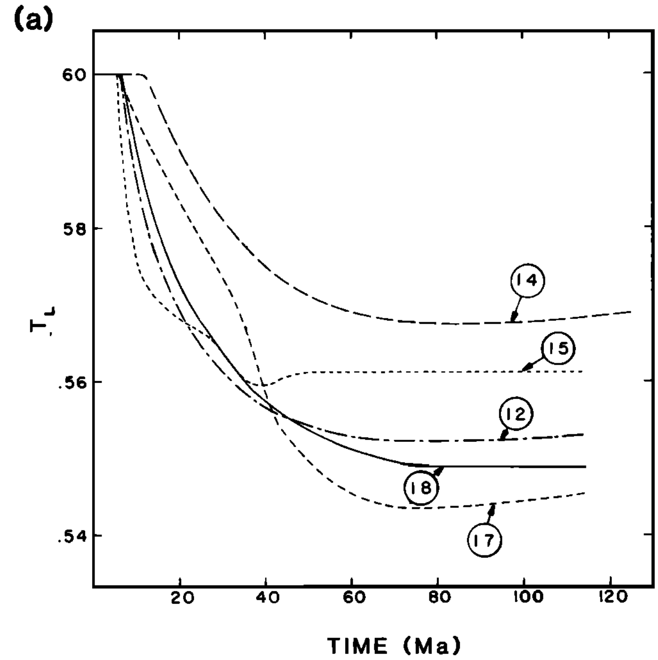

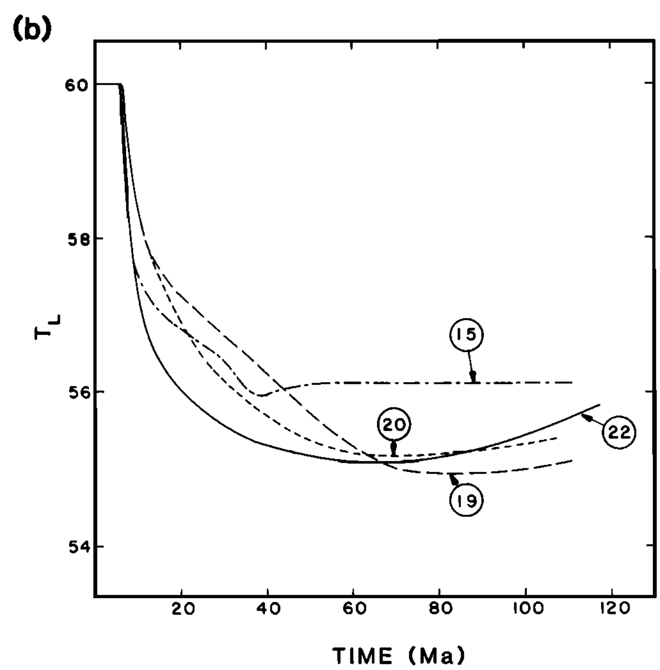

Fig. 5. Values of the average lid temperature T_L defined by equation (3), then normalized by the temperature at the base of the lid as a function of time for the cases indicated. Table 2 gives the parameters used in each case. The cases displayed in Figure 5b all have the same viscosity parameters but different box widths W, and case 15 had different initial conditions than the others. A value of nondimensionalized temperature of 0.60 corresponds to the conductive solution and a value of 0.50 corresponds to a linear temperature profile. Note that for times greater than 50 Ma the values of T_L are relatively constant.

the lid changes by less than 10%, the subsidence occurs primarily as a result of increasing Z_L. Convection changes the slope of the curves, but during most of the calculation they remain linear on such a plot. This dependence of Z_L on time can be written as

$$Z_L(t) = 2\lambda(\kappa t)^{1/2} \tag{5}$$

where κ is the thermal diffusivity. For purely conductive cooling, λ is given by $\mathrm{erf}^{-1}(0.9)$ [*Carslaw and Jaeger*, 1959]. For our models the value of λ will depend on the vigor of convection beneath the lid. A relationship between λ and the viscosity as well as other model parameters are given in a related paper [*Buck*, 1986]. $S(t)$ should depend on $\lambda\alpha T_m(\kappa t)^{1/2}$. The parameter λ is found to be proportional to the value of T_L. Values of λ determined from the present models are given in Table 2.

An alternative estimate of the subsidence is based on the change in the average temperature of the upper part of the box to a prescribed, constant depth of compensation [*Jarvis and Peltier*, 1982; *Houseman and McKenzie*, 1982; *Fleitout and Yuen*, 1984]. The material above the depth of compensation is assumed to be in isostatic equilibrium. The subsidence calculated using a depth of compensation of 150 km is effectively the same as that calculated from equation (4) because the change of temperature with time below the boundary layer is small compared to that in the conductive lid. The depth of compensation chosen affects the subsidence that is calculated from our model results. If the depth of compensation were taken to be at the bottom of the box, convective cooling would result in faster subsidence than conductive cooling.

The isostatic geoid anomaly [*Haxby and Turcotte*, 1978] is given by

$$H(t) = \frac{-2\pi G}{g}$$

$$= \left\{\frac{(\rho_m - \rho_w)[S(t)]^2}{2} + \alpha\rho_m \int_0^{Z_L} [T_m - T_h(z)]z\,dz\right\} \tag{6}$$

where $T_h(z)$ is the horizontally averaged temperature at a depth z. This expression is valid only if the density variation producing the anomaly is isostatically compensated and small in vertical compared to horizontal dimensions. Thus it should be valid as long as variations in temperature and therefore density, below the lithosphere are small as should be the case for the geoid offset across fracture zones.

The gravity anomaly at the top of the box is also calculated from our models. Three components contribute to the anomaly. One is due to temperature and therefore density variations in the box. A second is due to the deformation of the top surface of the box as a result of convective stresses. Third, vertical normal stress variations due to horizontal temperature differences within the conductive lid contribute to the deformation of the top boundary of the box. The first component of the anomaly is calculated by numerically integrating the following expression for the vertical component of gravity G_T due to distributed two-dimensional density anomalies:

$$G_T(x') = 2G\rho_m\alpha \int_0^D \int_{-2L}^{+3L} [T_h(z) - T(x, z)] \frac{z}{(x - x')^2 + z^2}\,dx\,dz \tag{7}$$

where G is the gravitational constant and the other values are as defined above. The temperature structure outside the box is assumed to be horizontally periodic with wavelength $2L$. The range of integration is over 2.5 wavelengths to avoid any edge effects.

To determine the component of the gravity anomaly due to the flow, we must calculate the normal stress σ_{zz} on the bottom boundary of the conductive lid. The normal stress at any boundary point is calculated using equations given by *McKenzie* [1977] and *Parmentier and Turcotte* [1978]. The stress at the surface of the box must include the effect of temperature and therefore vertical normal stress variations in the conductive lid (σ_T). Neglecting shear stresses on vertical

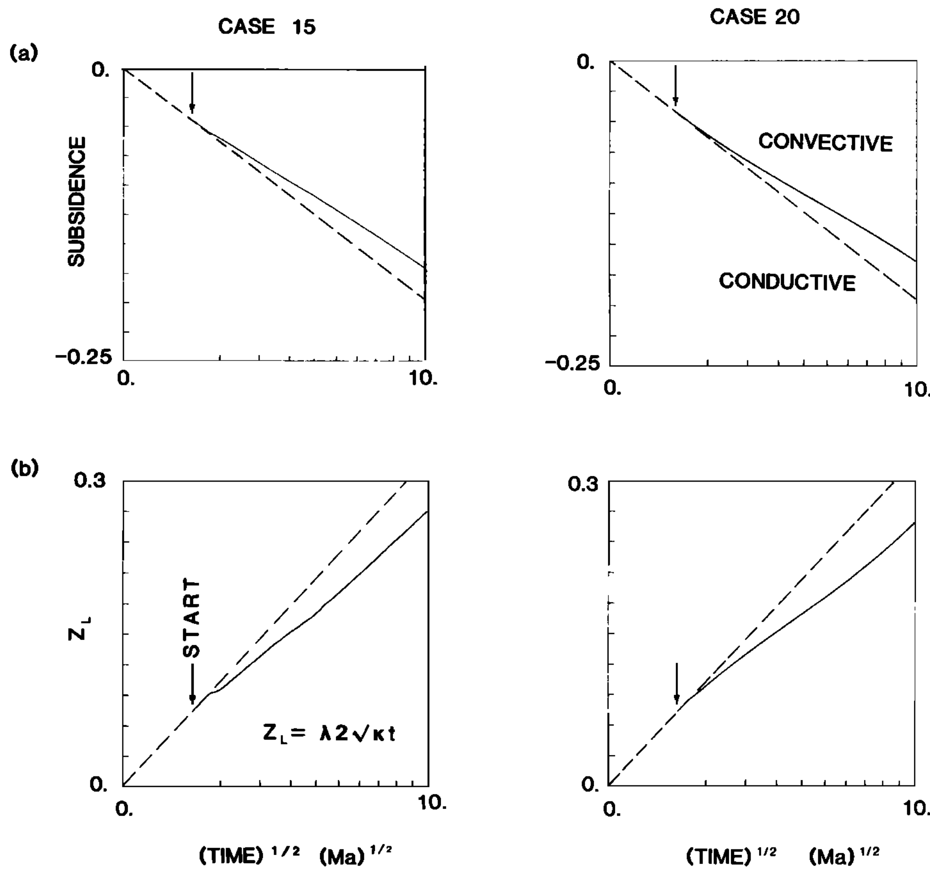

Fig. 6. The values of two parameters calculated for cases 15 and 20 plotted versus $t^{1/2}$. (*a*) The nondimensional value $(T_L - T_m)Z_L$ used to calculate the subsidence due thermal contraction within the lithosphere, as described in the text. (*b*) Z_L, the nondimensional depth to the bottom of the conductive lid.

planes within the lid, the total normal stress at the surface (σ_S) is the sum of σ_{zz} and σ_T. The stress at the surface is adjusted so that the average is zero. The gravitational effect of these stresses in our model is determined by the resulting elevation $E(x)$ of the surface. To determine this, we must assume a flexural rigidity D of the elastic lithosphere. If we assume D to be zero, resulting in a pointwise isostatic response, hydrostatic stresses due to elevation of the surface must match the normal stress at each point, giving

$$E(x) = \frac{\sigma_S(x)}{(\rho_m - \rho_w)g} \tag{8}$$

where g is the acceleration of gravity. If D is nonzero, the elevation will be reduced by an amount which depends on the wavenumber k of each Fourier component of the stress distribution. For an elastic layer thickness of 10 km and using values for elastic parameters from *Watts and Steckler* [1980], the flexural rigidity $D = 10^{23}$ kg m^2/s^2. For this flexural rigidity, a stress distribution with a wavelength less than 200 km produces almost no surface elevation according to the relation for the damping effect of a thin elastic layer [*McKenzie and Bowin*, 1976].

The gravity anomaly at a point above the surface due to an elevation anomaly is calculated assuming that the extra mass due to the surface elevation can be considered an infinite sheet at a depth of 4 km below the sea surface. This is a good approximation for features like those discussed here with a wavelength greater than several tens of kilometers. Then the total gravity anomaly caused by elevation is given by the sum of G_σ, which is the part of the signal produced by flow stresses (σ_{zz}), and G_L, which is the component due to the stresses produced by the temperature variations in the lithosphere (σ_T).

Finally, the average heat flux out of the top of the box ($Q_s(t)$) is given by the product of the average temperature gradient at $z = 0.$ and the conductivity K.

$$Q_s(t) = K \frac{1}{L} \int_0^L \left. \frac{dT}{dz} \right|_{(x,0)} dx \tag{9}$$

where dT/dz is estimated using a centered finite difference approximation.

RESULTS

The results of a calculation (case 15) within a box representing a 400 × 400 km region of the mantle are illustrated in Figure 3. Figure 3 shows several quantities which describe the flow at four times. The temperature contours give an idea of the rate of movement of cold sinking and hot rising material. Advective heat transfer dominates the conductive transfer in the region where isotherms are distorted from horizontal. The streamlines show the number of convection cells at a given time and the depth of penetration of the flow. The cells are seen to grow larger during the early part of the calculation. The initial wavelength of the flow is controlled by the thickness of the thermal boundary layer which first becomes unstable. *Jaupart* [1981] points out that the fastest growing wavelength of the instability for a boundary layer in which viscosity decreases exponentially with depth should be between π and 2π times the boundary layer thickness. The boundary layer defined here is the region where both the advective and conductive heat flux vary rapidly with depth. After 2 m.y., the wavelength of the flow in Figure 3 is about 60 km. This is consistent with an initial boundary layer thickness of about 10 km. In just another 2 m.y. the wavelength of the flow increases to nearly 120 km. The growth of the cells is rapid early in the calculation then later slows and finally stops when the box is filled. The slowing of the growth of the cells depends on the pressure dependence of the viscosity since this causes the viscosity to increase with depth. In a model where viscosity did not depend on pressure, the cells filled the box more rapidly than for any of the other cases.

The plots of the advective heat flux, shown for different times in Figure 3, exhibit some interesting features. For a model time of 2 m.y. the convection is just starting to develop and very little heat is being transported by the flow. At the next two times, 4 and 5 m.y. into the calculation, the plots of advective heat flux have an extra local maxima due to a large amount of cold material from the original unstable boundary layer moving down. The profiles of the advected heat flux for the rest of the calculation look more like that for case 20 shown in Figure 4. There the advective heat flux is a maximum at the base of the boundary layer and decreases monotonically with depth.

The horizontally averaged temperature profiles in Figure 3 show gradients in the conductive lid but relatively uniform temperature below the boundary layer. The difference between the horizontally averaged temperature at a given depth and the temperature which would result from purely conductive cooling at the same time is also shown. In the convecting region the temperatures are lower than they would be in the absence of convection, while in the conductive lid the temperatures are higher than they would be for purely conductive cooling.

The average temperature in the lid normalized by the temperature at the base of the lid (T_L), shown in Figure 5, is a measure of the temperature profile in the conductive lid. A value of T_L of 0.6 corresponds to purely conductive cooling and a value of 0.5 results from a linear temperature gradient reflecting steady state heat conduction. High heat flux from the convecting region results in a thinner lid in which temperatures more closely approximate the steady state distribution. For case 15, T_L decreases from the value for purely conductive cooling faster than for the other cases where only one convective wavelength is present in the box. The small cells, present early in the run for case 15, are more efficient in transferring heat out of the convecting region than are longer-wavelength cells. The local heat flux across the boundary layer at a given horizontal distance x from the center of upwelling between two cells should vary approximately as $x^{-1/2}$. Therefore the smaller the cell, the higher the horizontally averaged value of the heat flux across the boundary layer. After about 20 m.y. the value of T_L becomes remarkably constant.

The isostatic geoid anomaly $H(t)$ for case 15 as a function of time, calculated using equation (6), is shown in Figure 7 along with results for several other cases. The slope of these curves is proportional to $\lambda^2 \alpha T_m \kappa$ as shown by *Buck* [1986]. The slope is more appropriate for comparing with the data for the oceanic lithosphere. The time derivative of model geoid heights is also shown in Figure 7 along with the geoid-age slope [*Cazenave*, 1984] derived from the geoid height offset across oceanic fracture zones.

The total gravity anomaly associated with the small-scale convective rolls is shown in Figure 3, assuming no flexural damping of the signal. The amplitude of the anomalies increases with time, especially after the cells cease to grow very rapidly. This is because the effect of temperature variations in

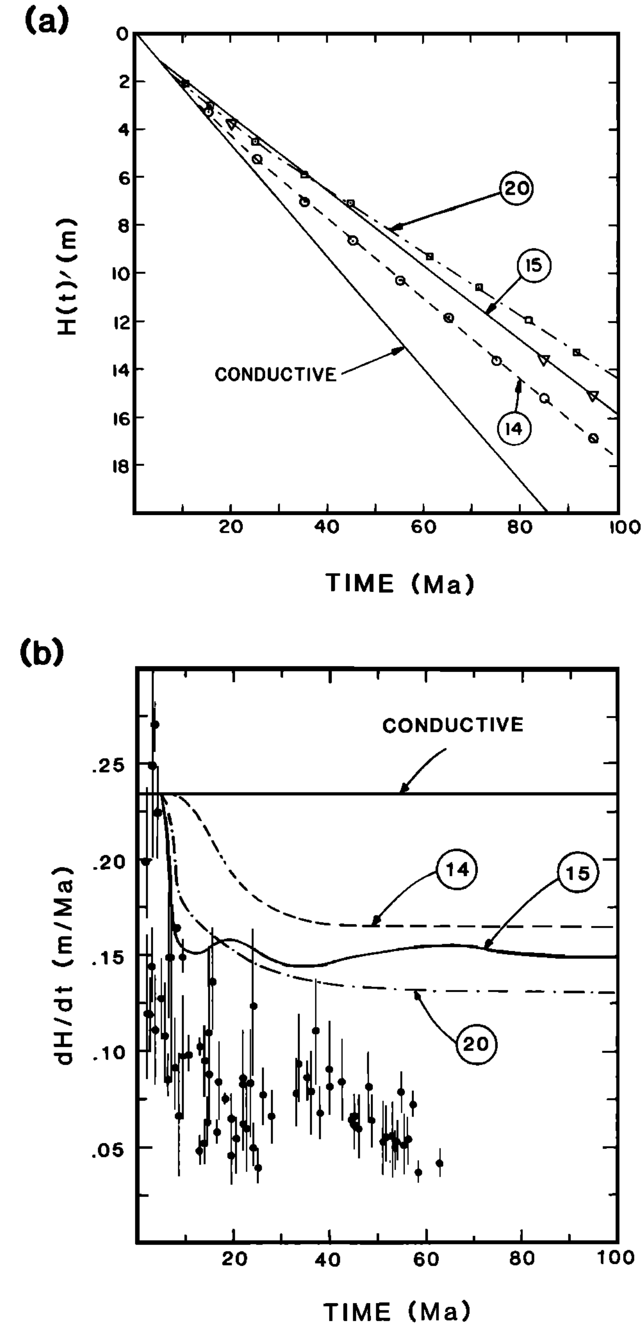

Fig. 7. (*a*) The variation of the isostatic geoid height H given by equation (6) with time for several of the cases including purely conductive cooling. (*b*) The values of the model geoid height slope (dH/dt) versus time. The slope can be related to a geoid-age slope derived from the observed geoid offset across fracture zones [*Cazenave*, 1984].

the lid lag the change in cell size since time is required for the lateral differences in advective heat flux to be conducted into the lid. The components which make up the total model gravity anomaly (G_σ, G_L, and G_T) are shown in Figure 8 at one time for case 15. Clearly, most of the total anomaly arises due to the combination of stresses at the base of the lithosphere (G_σ) and vertical normal stress variations through the lithosphere (G_L), both of which will be reduced in magnitude by the flexural rigidity of the elastic lithosphere. Admittance studies have not yet been done for the region of the Central Pacific studied by *Haxby and Weissel* [1986], but as shown in Figure 11, there is a positive correlation between gravity and topography as would be predicted by this model.

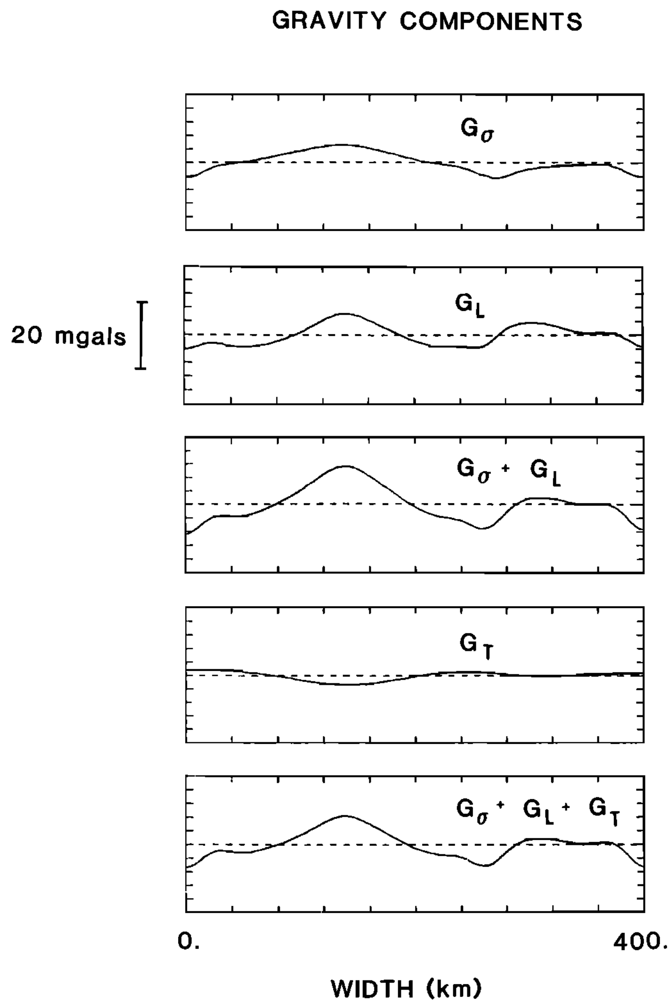

Fig. 8. The components of the model gravity signal described in the text for case 15 at a time 15 m.y. into the calculation. The component due to deviatoric stress and pressure variations at the base of the conductive lid is G_σ, that due to vertical normal stress variations in the lid is G_L, and that due to density variations throughout the box is G_T. No flexural damping of G_σ and G_L was included.

The magnitude of the maximum difference in peak to trough amplitude for the three components of the gravity signal are shown as a function of time for case 15 in Figure 9. Just as for the isostatic geoid anomaly the gravity anomaly changes most rapidly soon after the calculation is begun. The component of the signal due to the flow-induced stresses G_σ grows very quickly at first but later maintains a nearly constant value. The component resulting from lithospheric temperature variations G_L grows more slowly but continues to grow through most of the calculation. This is partly due to the increasing wavelength of the flow with time, which leads to a larger contrast in the local heat flux from the convection cell into the conductive lid. It also continues to increase with time after the cell width has become constant because as the lid thickens, the temperature variations extend over a greater depth. The magnitude of the signal arising from density contrasts throughout the box (G_T) is an almost constant fraction of G_L. The amplitude of G_T is much smaller than that of G_L and is opposite in sign from G_σ and G_L. The trend of G_T parallels G_L because most of that signal originates within the conductive lid.

A contour plot of the total model gravity signal is shown in Figure 10 for case 15. Distance is scaled with time through an assumed plate velocity of 4 cm/yr. Some of the profiles used to construct this figure are shown in Figure 3. No flexural damping was included. As seen before, the wavelengths of the signal increase with time, and the amplitude also increases somewhat.

Numerical calculations with the same boundary conditions as for the large box calculation (case 15) but with a periodic initial temperature perturbation were carried out for a number of cases which are listed in Table 2. To illustrate these one-cell calculations, the same quantities which were shown in Figure 3 for the large box calculation are shown in Figure 4 for case 20, which has the same viscosity parameters as case 15. Only one time is shown. The single convection cell starts out penetrating only part way through the depth of the box and goes through the stage of cell growth noted for case 15. Here there is no increase in the width of the cell; only its depth extent increases. For case 17, in which there was no pressure dependence of viscosity and so no viscosity increase with depth, cells rapidly filled the box, and slow downward penetration of the cell was not observed. This shows that the viscosity increase with depth is important in controlling the depth of penetration of convection cells and therefore the rate of increase of the convective wavelength.

In cases 17 and 19 the initial single cell broke down into two cells. Case 19 has the same viscosity parameters as case 20, but the width of the convecting region is twice as great (see Table 2). Case 17 has the same box size as case 20. Cell breakdown occurred because the initially preferred wavelength of instability was smaller than the box width.

Several general relations between the geophysical observables calculated for this set of models should be pointed out. One of the most obvious is that the rate of change of the temperature structure of the conductive lid varies inversely with the average viscosity in the boundary layer and also depends on the activation energy E. The convective heat flux controls the variation of the average lid temperature T_L with time (Figure 5). For case 14, which has an average viscosity 5 times that of case 20, T_L decreases more slowly from the conductive value. This same slow change is clearly seen in the rate of decrease in dH/dt shown in Figure 7 and in the slow increase in the amplitudes of the gravity components in Figure 9. For case 18, which has nearly the same initial viscosity in the region below the boundary layer but a lower activation energy E, growth is faster than for case 14. The decreased temperature dependence of viscosity for case 18 results in a larger heat flux to the base of the conductive lid.

As noted before, the size of the convection cells also affects the rate of heat transfer from the convecting region to the conducting lid. Case 22, which has a box half the width of case 20 but with all other parameters the same, showed a much faster decrease in T_L. The average advective heat flux for the smaller width box was greater by a factor of about $(2)^{1/2}$ when the viscosities were the same in the boundary layer region.

The average lid temperature T_L and the slope of the plot of the lid thickness versus $t^{1/2}$ remains constant for most of the calculations after about 30 m.y. of model time. This is a consequence of the negative feedback or self regulation of the convecting system [*Tozer*, 1965]. The higher the advective heat flux, the more quickly the convecting region cools. Cooling causes the viscosity to go up and the heat flux then goes down.

When T_L is nearly constant, the deviation of T_L from the conductive value (see Figure 5) varies inversely with the average viscosity. Since the rate of advective heat transfer is controlled by the average viscosity in the convecting region, the lower the viscosity, the higher the heat flux.

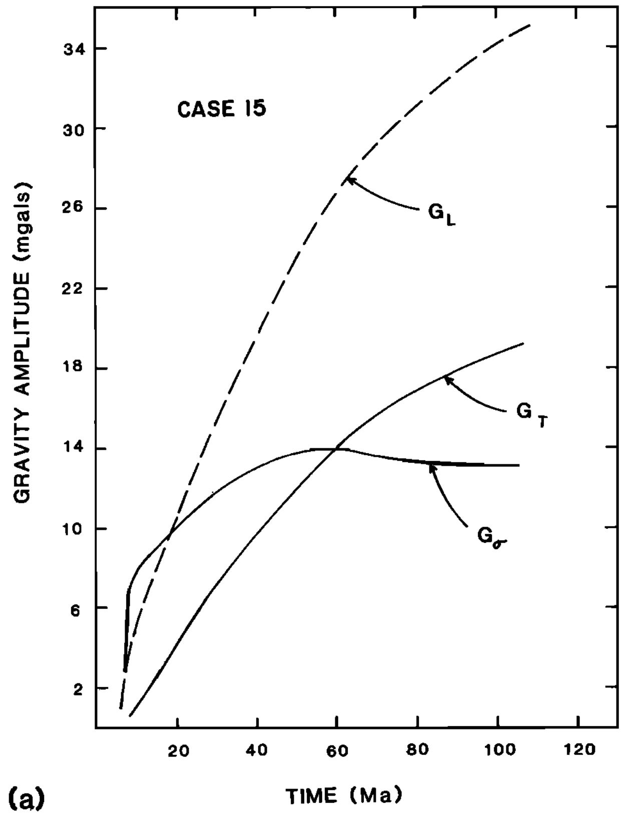

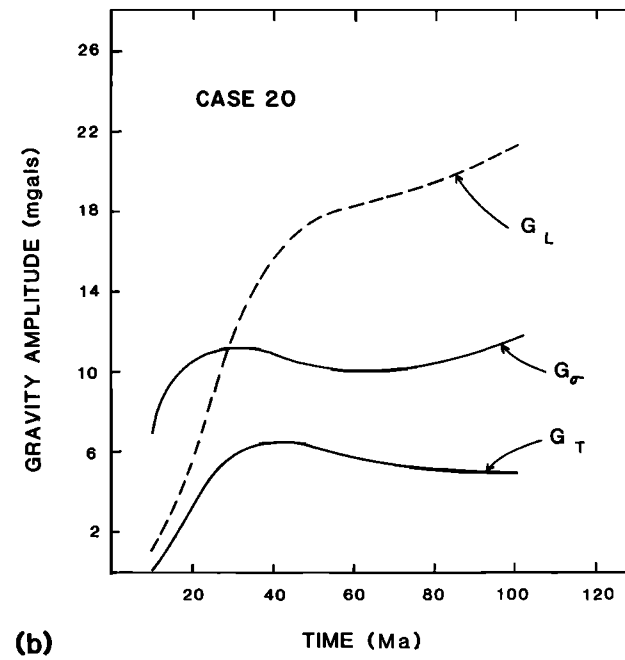

Fig. 9. The maximum peak-to-trough amplitude of the three components of the gravity signal, defined in the text, as they vary with time for two of the cases considered. G_σ and G_L are of the same sign, while G_T is opposite in sign. In case 15 the magnitude of the signals related to temperature variations, G_T and G_L, increase steadily with time as the wavelength of the cells grow. For case 20 the cell width is fixed, and the magnitude of these signals do not increase as rapidly.

The subsidence $S(t)$ is nearly linearly dependent on λ, and the isostatic geoid height $H(t)$ is proportional to λ^2. It is therefore important to consider the effect on λ of variations in the model parameters. Case 14, with the highest value of reference viscosity (Table 2) of all the cases, has the highest value of λ. It follows that this case also has the highest value of T_L, the highest rate of subsidence, and the largest average value of dH/dt. Decreasing the temperature dependence of viscosity, by lowering the activation energy E as in case 18, decreases λ. The average viscosity in the isothermal region is nearly the same at the start of the calculation for both case 14 and 18. However, for case 18 with a smaller E, the viscosity does not increase as rapidly as the convecting region cools. Therefore the advective heat flux does not decrease as rapidly as for case 14.

Lowering the pressure dependence of viscosity by reducing the activation volume V has much the same effect on λ as lowering the temperature dependence of the viscosity. As the depth to the base of the boundary layer increases with time of cooling, the viscosity there will be increasing because pressure is proportional to depth. The viscosity in the boundary layer controls the advective heat flux. Thus for case 17 where the activation volume V is small the heat flux decreases at a slower rate than it would if V were larger. Like increasing V, reducing the depth extent of the convective cooling increases the value of λ. This is shown by case 23 for which the depth of the box is 3/4 of that for the other cases.

The model parameters control the time variation of the gravity signal produced by convection in a way that does not scale simply with the parameter λ. The amplitude of the components (G_σ, G_L, and G_T) is shown for several of the models in Figure 9. One apparent result is that the component due to flow stresses (G_σ) is fairly constant in amplitude after an early period of change. The early rate of change of this signal is greater for the cases with lower viscosity in the convecting region. The magnitude of the constant level of G_σ does not vary much with average viscosity in the boundary layer region, but it is greater with a larger wavelength of the flow and with a smaller value of the activation energy E. The component of the gravity anomaly which depends on the stresses produced by temperature variations in the conductive lid G_L increases continuously with time for all the cases. The rate of increase is greater for the longer wavelength cases. Finally, the part of the gravity signal arising from density differences within the lid and convecting region G_T tends to parallel G_L but is generally lower in amplitude and opposite in sign.

DISCUSSION

The amplitudes and wavelengths of the gravity signals shown in Figure 3 for case 15 are in the range reported by *Haxby and Weissel* [1986] in their analysis of gravity features derived from Seasat altimetry data for the central east Pacific. The amplitude of the total gravity anomalies for all the small box calculations were also in this range for at least part of the time duration of the calculations. Figure 11 shows profiles of gravity and bathymetry perpendicular to the trend of linear gravity anomalies observed by Haxby and Weissel. The observed anomalies have a wavelength of 150–250 km and a peak-to-trough amplitude of 8–20 × 10^{-5} (m/s^2) over ocean floor older than 5 Ma. The highs and lows of these features make linear trends in the direction of plate motion.

Two important features of the calculated model gravity

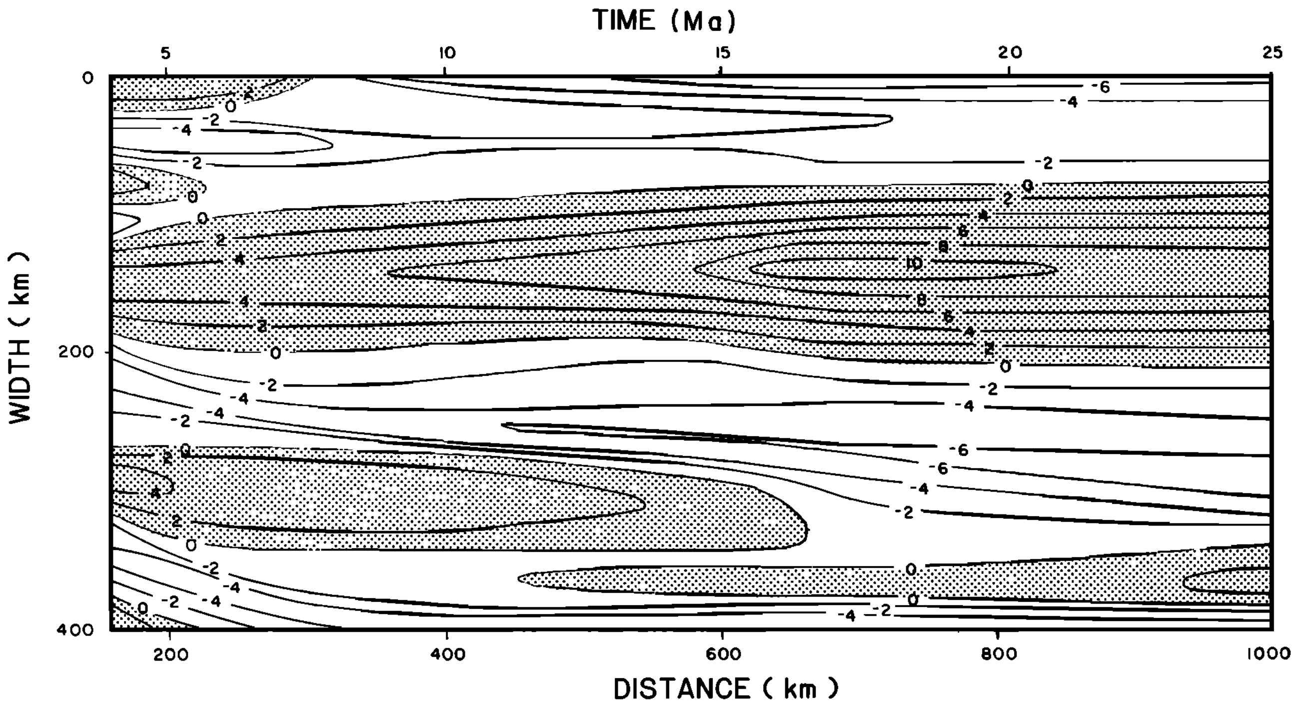

Fig. 10. Contour map of the total model gravity for case 15 for model times ranging from 4 to 25 m.y. after the start of the calculation. Regions of positive gravity anomaly are shaded. Time is related to distance by assuming a plate velocity of 4×10^{-2} m/yr. The contour interval is 2×10^{-5} m/s^2 (mGal). Flexural damping of the signals was not included. Note that the wavelength increases rapidly with time along with a moderate increase in the amplitude.

anomalies do not match the data. First, the increase in the wavelength of the anomalies with age observed by Haxby and Weissel is less than that predicted by the results of case 15 (see Figure 10). Second, when the effect of flexural damping due to the elastic lithosphere is included in the calculation of the model gravity signals, their amplitude for wavelengths less than 250 km become smaller than the observed signals. The elastic lithosphere will damp signals as a function of their wavelength. To illustrate this, we convolve a filter defined by *McKenzie and Bowin* [1976] with the model anomaly components G_σ and G_L to approximate the effect of the elastic lithosphere. Filtered model anomalies for different assumed values of the lithosphere thickness at one time for case 15 are shown in Figure 12. Using the elastic lithosphere thickness as a function of age, estimated by *Watts and Steckler* [1980], signals with wavelengths less than 250 km will be damped by more than 90% for lithosphere ages greater than 15 m.y. Only when the small-scale convective wavelengths are greater than 400–500 km will the effect of the elastic lithosphere in damping the signals of G_σ and G_L become small for all lithosphere ages.

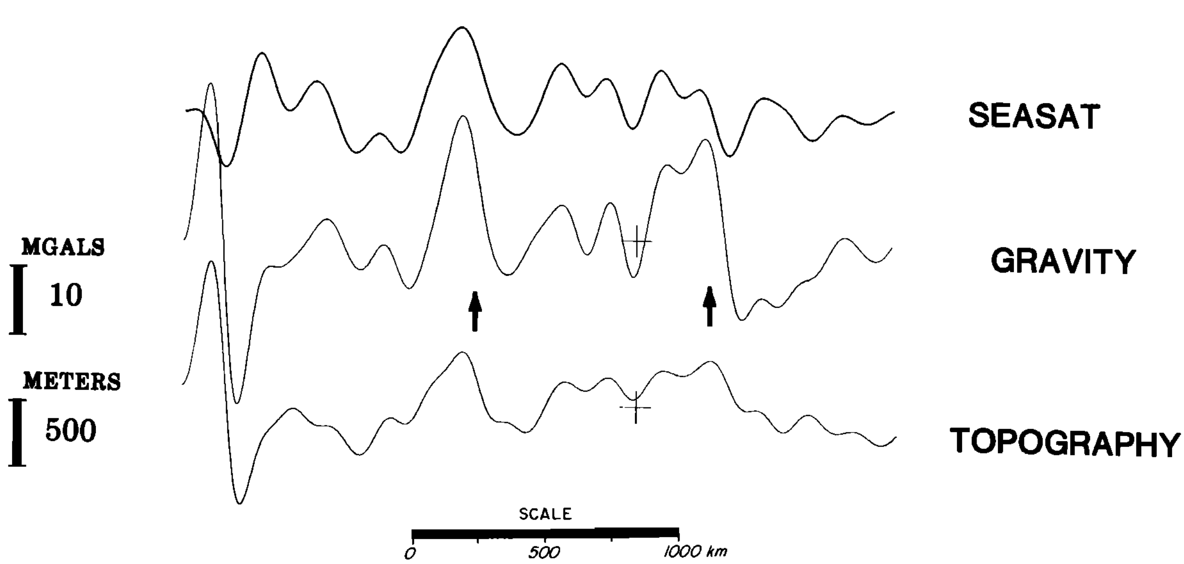

Fig. 11. Seasat-derived gravity anomalies, filtered shipboard gravity anomalies, and seafloor topography perpendicular to the trend of linear gravity highs and lows observed in Seasat data by *Haxby and Weissel* [1986]. These profiles are centered on 0°N latitude and 145°W longitude and are oriented roughly N-S. The shipboard gravity and topography has been filtered to remove signals with frequencies too high to be represented in Seasat data. Vertical arrows show the location of fracture zones.

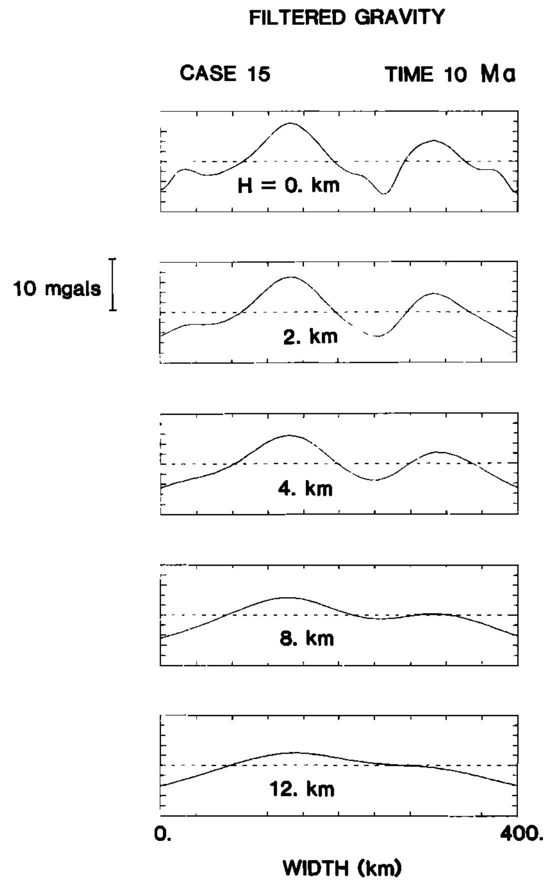

Fig. 12. The effect on the total model gravity signal ($G_\sigma + G_L + G_T$) of flexural damping due to elastic lithospheres of different thicknesses for a time of 10 m.y. into the calculation of case 15. The assumed thickness of the elastic lithosphere H is given at the top of each plot.

The elastic lithosphere acts to support topography in the same way that it suppresses the topographic expression of convective stresses. This may explain how small-scale convection can result in the observed pattern of short wavelength gravity anomalies. Topography produced by convection when the elastic lithosphere is thin can be "frozen" into the lithosphere as its thickness and therefore flexural rigidity increase with age. This topography and the associated gravity anomalies should not change greatly even as the convective pattern beneath the lithosphere changes. These gravity anomalies would have a linear trend in the direction of plate motion as do those observed. The stresses due to convection must be well developed before the flexural rigidity of the lithosphere is large enough to suppress their topographic expression. From the model results we estimate that this requires asthenosphere viscosities less than about 10^{18} Pa s under young oceanic lithosphere. Such values are not inconsistent with an estimated average mantle value of 10^{21} Pa s when the pressure dependence of viscosity is taken into account.

The calculated derivative of the model isostatic geoid height with time (Figure 7) reproduces the early trend in the data on geoid height offset across fracture zones. However, to match the magnitude of the change in $dH(t)/dt$ reported by *Cazenave* [1984] requires a lower viscosity than in any of the models considered here. Since the value of $dH(t)/dt$ should scale with $\lambda^2\kappa\alpha T_m$, it is possible to find a combination of these parameters which match both the average rate of subsidence and the rate of change of the isostatic geoid height. Another possibility is that the low observed values of $dH(t)/dt$ may be related to convection induced by differences in lithosphere thickness and horizontal temperature gradients across fracture zones. This may cause faster homogenization of the asthenosphere temperatures and lithosphere thicknesses in the vicinity of the fracture zone.

The surface heat flux $Q_s(t)$ should vary like $(T_m/\lambda)(Kc_p/t)^{1/2}$. Uncertainties in our knowledge of the conductivity K, the specific heat c_p [*Schatz and Simmons*, 1972; *Goranson*, 1942] and the measured values of heat flux are sufficiently large that data on oceanic heat flow can be matched by a variety of models including those presented here.

The comparison of the model results to data on the subsidence of the ocean basins is of great interest. For small-scale convection to be associated with the gravity and geoid features just discussed, it must develop in the first few million years after the lithosphere starts to cool. This means the onset of small-scale convection cannot produce the change in slope of the subsidence-age relation at about 70 Ma, as suggested by *Parsons and McKenzie* [1978] and *Houseman and McKenzie* [1982]. A number of alternative explanations for this feature of the subsidence data have been given [*Forsyth*, 1975; *Schubert et al.*, 1976; *Parmentier and Turcotte*, 1977; *Heestand and Crough*, 1981; *Jarvis and Peltier*, 1982; *Fleitout and Yuen*, 1984], all involving a heat flux from the mantle brought to the base of the lithosphere by either convection or conduction.

Our main interest is the early evolution of the oceanic lithosphere where the effect of a heat flux from deeper in the mantle should be negligible. We have shown that the rate of subsidence due to vertical thermal contraction in the lithosphere should depend on $\lambda\alpha T_m(\kappa t)^{1/2}$ for cooling of the mantle in the absence of heat sources. The average subsidence of the North Atlantic and the North Pacific ocean basins as estimated by *Parsons and Sclater* [1977] can be fit by a model with viscosities low enough to produce the gravity signals discussed above. Since the cooling of the asthenosphere may affect the subsidence, further work is being done to relate predictions of this model to data.

CONCLUSIONS

These calculations have shown that small-scale convection can produce the magnitude of the short-wavelength gravity anomalies observed for at least one area of the oceanic lithosphere and can also be consistent with seafloor subsidence data. Subsidence that is linear with $t^{1/2}$ is reproduced by model results, but the rate of subsidence depends on the vigor of the small-scale convection. Oceanic heat flow can also be fit with a model which includes small-scale convection. The geoid height offsets across fracture zones is more nearly matched by our results than by a model that includes only conductive cooling. The effect of convection due to differences in lithosphere thickness across fracture zones may explain the geoid data more completely.

If small-scale convection can explain observed short-wavelength gravity anomalies in the oceans, two things are required. First, convection must begin in the first few million years after formation of the lithosphere at a mid-ocean ridge. In this case, viscosities beneath the lithosphere must have a minima around 10^{18} Pa s. Second, topography, which gives rise to the observed gravity anomalies, must be produced by the stresses associated with convection when the elastic lithosphere was thin enough that it could be easily deformed. Our models also show that the vertical and horizontal scales of small-scale convection beneath the lithosphere increase with time. This would result in a much larger increase in the wavelength of the gravity anomalies than is observed. Topography must be supported by the strength of the elastic lithosphere as it cools and thickens, and to preserve a relatively constant wavelength, it must be "frozen in."

Acknowledgments. Thanks to Nafi Toksoz for support in doing this work. Discussions with Barry Parsons and the reviews of Luce Fleitout and Ulrich Christensen improved the manuscript. W.R.B. was supported on an Exxon Teaching Fellowship and a Lamont postdoctoral fellowship. E.M.P. was partially supported by NASA grant NAG 5-50 and National Science Foundation grant OCE-82-08634.

REFERENCES

Batchelor, G. K., *An Introduction to Fluid Dynamics*, Cambridge University Press, New York, 1967.

Buck, W. R., Small scale convection and the evolution of the lithosphere (abstract), *Eos Trans. AGU*, *64*, 309, 1983.

Buck, W. R., Parameterization of the effects of convection in a variable viscosity fluid with application to the earth, *Geophys. J. R. Astron. Soc.*, in press, 1986.

Carslaw, H. S., and J. C. Jaeger, *Conduction of Heat in Solids*, 510 pp., Oxford University Press, New York, 1959.

Cathles, L. M., III, *The Viscosity of the Earth's Mantle*, 341 pp., Princeton University Press, Princeton, N. J., 1975.

Cazenave, A., Thermal cooling of the oceanic lithosphere: New constraints from geoid height data, *Earth Planet. Sci. Lett.*, *70*, 395–406, 1984.

Curlet, N. W. E., Experimental and numerical modelling of natural convection in an enclosure, Ph.D. thesis, Mass. Inst. of Technol., Cambridge, 1976.

Fleitout, L., and D. Yuen, Secondary convection and the growth of the oceanic lithosphere, *Phys. Earth Planet. Inter.*, *36*, 181–212, 1984.

Forsyth, D. W., The early structural evolution and anisotropy of the oceanic upper mantle, *Geophys. J. R. Astron. Soc.*, *43*, 103–162, 1975.

Gage, K., and W. Reid, The stability of thermally stratified Poiseille flow, *J. Fluid Mech.*, *33*, 21–32, 1968.

Goetze, C., The mechanisms of creep in olivine, *Philos. Trans. R. Soc. London, Ser. A*, *288*, 99–119, 1978.

Goranson, R. W., Heat capacity: Heat of fusion, Handbook of Physical Constants, *Geol. Soc. Am. Spec. Pap.*, *36*, 223–242, 1942.

Graham, A., Shear patterns in an unstable layer of air, *Philos. Trans. R. Soc. London, Ser. A*, *232*, 285–296, 1933.

Haxby, W. F., and D. L. Turcotte, On isostatic geoid anomalies, *J. Geophys. Res.*, *83*, 5473–5478, 1978.

Haxby, W. F., and J. K. Weissel, Evidence for small-scale convection from Seasat altimeter data, *J. Geophys. Res.*, in press, 1986.

Heestand, R. L., and S. T. Crough, The effect of hotspots on the ocean age-depth relation, *J. Geophys. Res.*, *86*, 6107–6114, 1981.

Houseman, G. A., and D. P. McKenzie, Numerical experiments on the onset of convective instability in the earth's mantle, *Geophys. J. R. Astron. Soc.*, *68*, 133–164, 1982.

Ingersoll, A., Convective instabilities in plane Couette flow, *Phys. Fluids*, *9*, 682–689, 1966.

Jarvis, G. T., and W. R. Peltier, Mantle convection as a boundary layer phenomena, *Geophys. J. R. Astron. Soc.*, *68*, 389–427, 1982.

Jaupart, C., On the mechanisms of heat loss beneath continents and oceans, Ph.D. thesis, 215 p., Mass. Inst. of Technol., Cambridge, 1981.

Jaupart, C., and B. Parsons, Convective instabilities in a variable viscosity fluid cooled from above, *Phys. Earth Planet. Inter.*, *39*, 14–32, 1985.

Kohlstedt, D. L., H. P. K. Nichols, and P. Hornack, The effect of pressure on the rate of dislocation recovery in olivine, *J. Geophys. Res.*, *85*, 3125–3130, 1980.

McKenzie, D. P., Surface deformation, gravity anomalies and convection, *Geophys. J. R. Astron. Soc.*, *48*, 211–238, 1977.

McKenzie, D. P., and C. Bowin, The relationship between bathymetry and gravity in the Atlantic Ocean, *J. Geophys. Res.*, *81*, 1903–1916, 1976.

Parmentier, E. M., Studies of thermal convection with application to convection in the earth's mantle, Ph.D. thesis, Cornell Univ., Ithaca, N. Y., 1975.

Parmentier, E. M., and D. L. Turcotte, Two dimensional mantle flow beneath a rigidly accreting lithosphere, *Phys. Earth Planet. Inter.*, *17*, 281–289, 1978.

Parsons, B., and D. McKenzie, Mantle convection and the thermal structure of plates, *J. Geophys. Res.*, *83*, 4485–4496, 1978.

Parsons, B., and J. G. Sclater, An analysis of the variation of ocean floor bathymetry and heat flow with age, *J. Geophys. Res.*, *82*, 803–827, 1977.

Passey, Q. R., Upper mantle viscosity derived from the difference in rebound of the Provo and Bonneville shorelines: Lake Bonneville basin, Utah, *J. Geophys. Res.*, *86*, 11701–11708, 1981.

Peltier, W. R., and J. T. Andrews, Glacial isostatic adjustment, I, the forward problem, *Geophys. J. R. Astron. Soc.*, *46*, 605–646, 1976.

Richter, F. M., Convection and the large-scale circulation of the mantle, *J. Geophys. Res.*, *78*, 8735–8745, 1973.

Richter, F. M., and D. McKenzie, Simple plate models of mantle convection, *J. Geophys.*, *44*, 441–471, 1978.

Richter, F. M., and B. Parsons, On the interaction of two scales of convection in the mantle, *J. Geophys. Res.*, *80*, 2529–2541, 1975.

Ringwood, A. E., *The Composition and Petrology of the Earth's Mantle*, 618 pp., McGraw-Hill, New York, 1975.

Roache, P. J., *Computational Fluid Dynamics*, 466 pp., Hermosa, Albuquerque, N. M., 1982.

Sammis, C. G., J. C. Smith, and G. Schubert, A critical assessment of estimation methods for activation volume, *J. Geophys. Res.*, *86*, 10707–10718, 1981.

Schatz, J. F., and G. Simmons, Thermal conductivity of earth materials at high temperature, *J. Geophys. Res.*, *77*, 6966–6983, 1972.

Schubert, G., C. Frodevevaux, and D. A. Yuen, Oceanic lithosphere and asthenosphere: Thermal and mechanical structure, *J. Geophys. Res.*, *81*, 3525–3540, 1976.

Sclater, J. G., and J. Francheteau, The implications of terrestrial heat flow observations on current tectonic and geochemical models of the crust and upper mantle of the earth, *Geophys. J. R. Astron. Soc.*, *20*, 509–542, 1970.

Tozer, D. C., Heat transfer and convection currents, *Philos. Trans. R. Soc. London, Ser. A*, *258*, 252–271, 1965.

Turcotte, D. L., K. E. Torrance, and A. T. Hsui, Convection in the earth's mantle, *Methods Comput. Phys.*, *13*, 431–454, 1973.

Watts, A. B., and M. S. Steckler, Observations of flexure and the state of stress in the oceanic lithosphere, *J. Geophys. Res.*, *85*, 6369–6376, 1980.

Weertman, J., and J. R. Weertman, High temperature creep of rock and mantle viscosity, *Annu. Rev. Earth Planet. Sci.*, *3*, 293–315, 1975.

Weins, D. A., and S. Stein, Implications of oceanic intraplate seismicity for plate stresses, driving forces and rheology, *Tectnophysics*, *116*, 143–162, 1985.

Yuen, D. A., and L. Fleitout, Stability of the oceanic lithosphere with variable viscosity: An initial-value approach, *Phys. Earth Planet. Inter.*, *34*, 173–185, 1984.

Yuen, D. A., W. R. Peltier, and G. Schubert, On the existence of a second scale of convection in the upper mantle, *Geophys. J. R. Astron. Soc.*, *65*, 171–190, 1981.

W. R. Buck, Lamont-Doherty Geological Observatory, Palisades, NY 10964.

E. M. Parmentier, Department of Geological Sciences, Brown University, Providence, RI 02912.

(Received February 15, 1985;
revised October 29, 1985;
accepted October 31, 1985.)